Nano Research

Open Access

Research Article

Synergistic copper single-atoms and nanoparticles *in-situ* generated towards nitrate electroreduction to ammonia

Zirui Liu[1,§], Jiacheng Jayden Wang[2,3,§], Yifan Li[1], Chenglong Qiu[2], Yunhong Liang[1]✉, and Jiacheng Wang[2]✉

[1] *The Key Laboratory of Bionic Engineering, Ministry of Education, Jilin University, Changchun 130025, China*
[2] *Zhejiang Key Laboratory for Island Green Energy and New Materials, Institute of Electrochemistry, School of Materials Science and Engineering, Taizhou University, Taizhou 318000, China*
[3] *State Key Laboratory of High-Performance Ceramics and Superfine Microstructure, Shanghai Institute of Ceramics, Chinese Academy of Sciences, Shanghai 200050, China*
§ *Zirui Liu and Jiacheng Jayden Wang contributed equally to this work.*

Cite this article: *Nano Research*, **2026**, *19*, 94908370. https://doi.org/10.26599/NR.2026.94908370

ABSTRACT: Electrocatalytic synthesis of ammonia (NH_3) from nitrate (NO_3^-) is an effective approach for reducing nitrate pollutants in the environment and a promising method for ammonia synthesis under mild conditions. However, current catalyst syntheses are costly, and their application in real wastewater remains underexplored. Herein, we prepared high-efficiency copper-based single-atom-nanoparticle synergistic sites on carbon felt ($Cu_{SA/NP}$@C) from copper-containing wastewater. Trace Cu^{2+} in wastewater enables efficient nitrate reduction reaction (NO_3RR), and the effect of different Cu^{2+} concentrations was also investigated. The optimized $Cu_{SA/NP}$@C, with synergy between single atoms and nanoparticles, shows excellent activity: a maximum Faradaic efficiency of ~ 100% (at −0.3 V vs. reversible hydrogen electrode (RHE)) and a NH_3 yield of ~ 10 mg·cm^{-2}. Theoretical calculations reveal that Cu single-atoms and nanoparticles synergistically act on the NO_3* and H* intermediates to promote nitrate hydrogenation to NH_3. A membrane electrode assembly with the $Cu_{SA/NP}$@C cathode achieves the NH_3 synthesis at an industrial current density of 200 mA·cm^{-2} for over 90 h. This "treating waste with waste" strategy offers new paths for nitrate wastewater recycling and green NH_3 synthesis advancement.

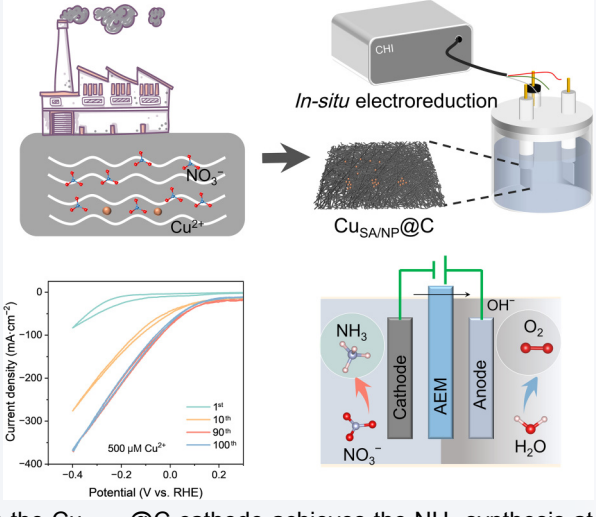

KEYWORDS: nitrate reduction, ammonia synthesis, copper nanoparticles, single-atom sites, resource recycling

1 Introduction

Ammonia (NH_3), one of the chemicals with the highest global production, possesses the dual attributes of being an important chemical raw material and a renewable energy carrier [1, 2]. Currently, industrial NH_3 synthesis mainly relies on the Haber–Bosch process at high temperatures and pressure (~ 500 °C, > 100 atm), which not only has high energy consumption, but also is accompanied by significant CO_2 emissions (400 Mt) every year [3, 4]. Thus, the development of green alternative technologies for ammonia production is urgently needed [5–7]. Although the electrocatalytic nitrogen reduction reaction (NRR) is an environmentally friendly ammonia production route, its prominent drawbacks including the extremely low solubility of nitrogen (N_2) and the high bond energy of N≡N (941 kJ·mol^{-1}) [8, 9], and the competitive hydrogen evolution reaction (HER) at the cathode lead to an exceptionally low ammonia yield, which inhibits the large-scale production of ammonia [10]. Nitrate (NO_3^-) has become an ideal raw material for electrochemical ammonia synthesis due to its high water solubility and relatively low N=O dissociation energy (204 kJ·mol^{-1}) [11, 12]. Meanwhile, NO_3^- is widely present in

Received: September 24, 2025; **Revised:** November 27, 2025
Accepted: December 23, 2025

✉Address correspondence to Jiacheng Wang, jiacheng.wang@tzc.edu.cn; Yunhong Liang, liangyunhong@jlu.edu.cn

polluted systems such as industrial wastewater, nuclear waste liquid, and groundwater [13–15], endowing its conversion process with the dual values of environmental remediation and resource recovery. However, considering that NO_3RR is a complex process involving 8 electrons and 9 protons, the development of high-performance electrocatalysts with high ammonia selectivity and activity is urgently required [16–18].

Copper-based materials show broad application prospects in the electrochemical nitrate reduction reaction (NO_3RR) due to their low cost, non-toxicity, and excellent catalytic activity [19–22]. Although a variety of artificially synthesized copper-based catalysts have exhibited good performance, their complex preparation processes and high costs restrict large-scale applications [23, 24]. This study takes a different approach and innovatively uses Cu^{2+} (with a concentration of approximately 100–1000 $mg{\cdot}L^{-1}$) in electroplating wastewater as a raw material to convert pollutants into catalytically active species, realizing resource recycling. Considering that the NO_3RR pathway involves multiple nitrogen-oxygen intermediates and is easily interfered by HER, the interface design of the catalyst is of crucial importance [25, 26].

A large number of previous studies have shown that the construction of a multi-level structure of nanoclusters is one of the effective ways to provide a high specific surface area, generate more active sites, and improve the activity of electrocatalysts [27–31]. Given the multi-step nature and the involvement of multiple intermediates in NO_3RR, it is imperative to rationally design electrocatalysts with synergistic active sites, as possible is essential to enhance the activity and selectivity of NO_3RR.

In this work, a copper-based electrocatalyst with synergistic single-atom and nanoparticulate sites on carbon felt (CF) ($Cu_{SA/NP}$@C) was directly prepared via *in-situ* electrochemical deposition using copper-containing wastewater as the precursor, showing high activity and selectivity for NO_3RR to ammonia synthesis. Systematic investigation of Cu^{2+} concentrations reveals that the optimal catalyst fabricated at 500 μM exhibits a NH_3 Faradaic efficiency (FE) of ~ 100% and a NH_3 yield of 10 $mg{\cdot}cm^{-2}$ at −0.3 V vs. reversible hydrogen electrode (RHE), owing to the synergistic effect between Cu_{SA} and Cu_{NP}. Density functional theory (DFT) calculations and *in-situ* characterizations further clarify that these two active components could work in tandem, with Cu single atoms regulating *H behavior and nanoparticles lowering reaction energy barriers, collectively promoting NO_3RR. Moreover, a membrane electrode assembly (MEA) based on this $Cu_{SA/NP}$@C catalyst achieves stable NH_3 synthesis at an industrial-level current density of 200 $mA{\cdot}cm^{-2}$ for over 90 h. This work not only realizes "treating waste with waste and turning waste into treasure", but also provides a new path for nitrate wastewater recycling and the advancement of green ammonia synthesis.

2 Results and discussion

2.1 Synthesis and structure characterization of $Cu_{SA/NP}$@C

The copper single-atom-nanoparticle catalyst was first prepared via *in-situ* electrochemical deposition on carbon felt ($Cu_{SA/NP}$@C), as schematically illustrated in Fig. 1(a) (details in Section 4 and Figs. S1 and S2 in the Electronic Supplementary Material (ESM)). Figure 1(b) presents the evolutive cyclic voltammetry (CV) curves of carbon felt measured in 1 M KOH electrolyte containing 0.1 M KNO_3 and 500 μM Cu^{2+}, recorded from the 1st to 100th cycles. Notably, the current density at −0.4 V versus RHE exhibits a significant upward trend with increasing cycle numbers, and this enhancement continues until the 100th cycle. This phenomenon clearly indicates that the presence of Cu^{2+} contributes to the activity improvement of the carbon felt.

$Cu_{SA/NP}$@C obtained at the Cu^{2+} concentration of 500 μM Cu^{2+} was further analyzed by high-resolution transmission electron microscopy (HRTEM). HRTEM images of the $Cu_{SA/NP}$@C exhibit the coexistence state of single atoms and nanoparticles (Figs. 1(c) and 1(d), and Fig. S3 in the ESM), indicating a certain synergistic effect. The $Cu_{SA/NP}$@C sample shows lattice fringes with a *d*-spacing of 2.08 Å, which corresponds to Cu (111) and lattice stripes of 0.208 and 0.209 nm also correspond to the (111) facet of Cu (Figs. 1(e) and 1(g)) [32]. X-ray photoelectron spectroscopy (XPS) was employed to analyze the presence and chemical states of copper in the $Cu_{SA/NP}$@C catalyst [33–35]. The high-resolution Cu 2p XPS spectrum exhibits only weak Cu^{2+} features, consistent with the extremely low loading and dispersion of Cu as single atoms, and likely exacerbated by partial oxidation upon air exposure [36, 37]. In the Raman spectrum, the ν(Cu–O) vibration is characterized by two distinct peaks at around 625 and 714 cm^{-1}, and the characteristic peak of CuO centers at 298 cm^{-1} (Fig. 1(g)) [38]. The copper content (wt.%) was measured using inductively coupled plasma optical emission spectroscopy (ICP-OES),and the results showed that the carbon felt contained only a tiny amount of copper (0.003 wt.%, Table S1 in the ESM). The above description confirms that Cu^{2+} (e.g., those derived from wastewater) can successfully undergo *in-situ* electrochemical transformation, thereby generating the $Cu_{SA/NP}$@C catalyst. This catalyst is characterized by the coexistence of single atoms (Cu_{SA}) and nanoparticles (Cu_{NP}), and serves as an efficient active component for NO_3RR to ammonia synthesis.

2.2 Synergistic properties for $Cu_{SA/NP}$@C

To investigate the synergistic effect between copper single atoms (Cu_{SA}) and copper nanoparticles (Cu_{NP}) in the $Cu_{SA/NP}$@C catalyst, as well as the electronic states of surface-adsorbed intermediates, charge density difference (CDD) calculations were first performed. Based on the results of structural characterizations, the models of Cu_{SA} and Cu_{NP} were constructed (Fig. 2(a)), with detailed simulation parameters provided in Section 4. Notably, NO_3 adsorbs on Cu_{SA} via single Cu active site but adsorbs on Cu_{NP} via dual-Cu-site adsorption configuration (Cu_1-O_1: 1.941 Å and Cu_2-O_2: 1.941 Å) (Figs. 2(b) and 2(c)). The CDD diagram indicates that the Cu_{NP} surface shows charge accumulation (yellow) and depletion (cyan), implying the faster transfer of electrons from Cu to NO_3, which is beneficial for the NO_3 ion entrapment. The band center model served as a robust methodology for examining the binding energy and catalytic interactions between transition metals and reactants or intermediates. In the Cu_{NP} model, Cu atoms possess a d-band center closer to the Fermi level (Figs. 2(d) and 2(e)). Moreover, the density of states (DOS) analysis shows more significant overlap between Cu and O orbitals in NO_3*-adsorbed Cu_{NP} compared to Cu_{SA}, which confirms a stronger Cu–O bond strength on Cu_{NP}. Importantly, the dual-Cu-site binding mode of NO_3* on Cu_{NP} enables N–O bond cleavage under subsequent proton attack. Figure 2(f) presents the water splitting free energy diagram for Cu_{SA} and Cu_{NP}. The results indicate that Cu_{NP} exhibits stronger water adsorption energy (−0.126 eV) than Cu_{SA} (0.282 eV), implying that Cu_{NP} is more capable of supplying active protons to

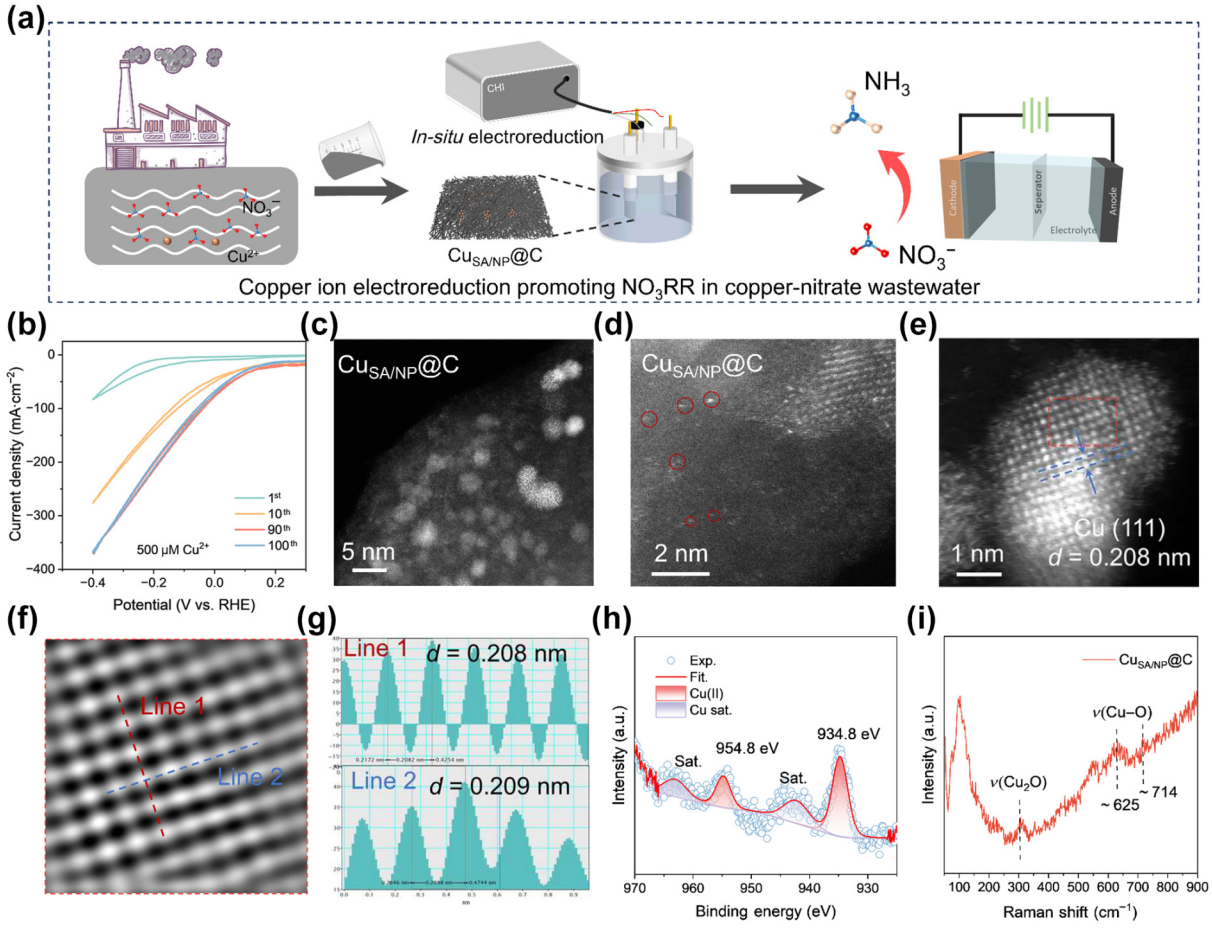

Figure 1 *In-situ* copper ion electroreduction promoting NO_3RR in copper-containing nitrate wastewater. (a) Schematic of constructing $Cu_{SA/NP}@C$ as the cathode for efficient NO_3RR from copper-containing wastewater. (b) CV curves for preparing $Cu_{SA/NP}@C$ in 1 M KOH containing 0.1 M KNO_3 with 500 μM Cu^{2+}. (c)–(f) High-resolution transmission electron microscopy (HRTEM) images of $Cu_{SA/NP}@C$. (h) Cu 2p XPS spectrum of $Cu_{SA/NP}@C$. (i) Raman spectrum of $Cu_{SA/NP}@C$.

facilitate the protonation process in NO_3RR. In contrast, Cu_{SA} does not spontaneously adsorb water, which helps inhibit the competing HER.

Further insights from the configurations of adsorbed water and adsorbed hydrogen (*H) show that Cu_{SA} can modulate water adsorption behavior (Fig. 2(g)), suppress the dimerization of *H to form H_2, and thus enhance the selectivity toward the target NH_3. Thus, under the collaborative regulation of Cu_{SA} and Cu_{NP}, the $Cu_{SA/NP}@C$ catalyst destabilizes H species, shifting their reaction pathway toward combination with nitrogen-oxygen intermediates (NO_x) rather than H_2 formation, thereby promoting the generation of NH_3 in NO_3RR.

2.3 Electrocatalytic NO_3RR performance of $Cu_{SA/NP}@C$

To evaluate the electrochemical performance of the CuSA/NP@C catalyst toward NO_3RR, linear sweep voltammetry (LSV) tests were first conducted on the *in-situ* prepared $Cu_{SA/NP}@C$ electrode in a 1 M KOH electrolyte containing 0.1 M KNO_3 at 25 °C (Fig. 3(a) and details in Section 4). As shown in Fig. 3(b), the $Cu_{SA/NP}@C$ catalyst exhibits a larger current density than pure carbon felt across all investigated overpotentials, which directly confirms the superior NO_3RR activity of $Cu_{SA/NP}@C$. Subsequently, the influence of precursor Cu^{2+} concentration on the NO_3RR performance was systematically compared and analyzed. The results reveal that the NO_3RR performance improves with increasing Cu^{2+} concentration; when the Cu^{2+} concentration reaches 500 μM, the catalytic performance basically plateaus (Fig. 3(c) and Fig. S4 in the ESM). Therefore, the catalyst prepared under this optimal Cu^{2+} concentration (500 μM) was designated as $Cu_{SA/NP}@C$ for subsequent characterizations and tests. The electrochemical impedance spectroscopy (EIS) and the Tafel slopes all indicate a faster charge transfer rate for $Cu_{SA/NP}@C$ (Fig. 3(d) and Fig. S5 in the ESM). In terms of product selectivity and yield, $Cu_{SA/NP}@C$ outperforms carbon felt at all tested potentials, exhibiting higher FE for NH_3 and higher NH_3 yield. Specifically, for the $Cu_{SA/NP}@C$ catalyst, the maximum NH_3 FE reaches ~ 99.0% at –0.3 V vs. RHE, and the corresponding NH_3 yield is as high as 10 $mg \cdot h^{-1} \cdot cm^{-2}$ at the same potential, both of which are significantly higher than those for carbon felt (Figs. 3(e) and 3(f), and Fig. S6 in the ESM). Meanwhile, we conducted the stability tests of $Cu_{SA/NP}@C$ in a three-electrode system at 50 $mA \cdot cm^{-2}$ for 10 h (Fig. 3(g), and Figs. S7 and S8 in the ESM). Throughout the test, the catalyst maintains a stable potential of approximately 0.0 V vs. RHE without obvious degradation, indicating its excellent electrochemical stability and promising prospects for practical NO_3RR applications.

2.4 NO_3RR mechanism analysis for $Cu_{SA/NP}@C$

The NO_3RR mechanism of $Cu_{SA/NP}@C$ was further investigated by various techniques. *In-situ* Fourier transform infrared (FT-IR) spectroscopy was performed to detect the intermediates and track

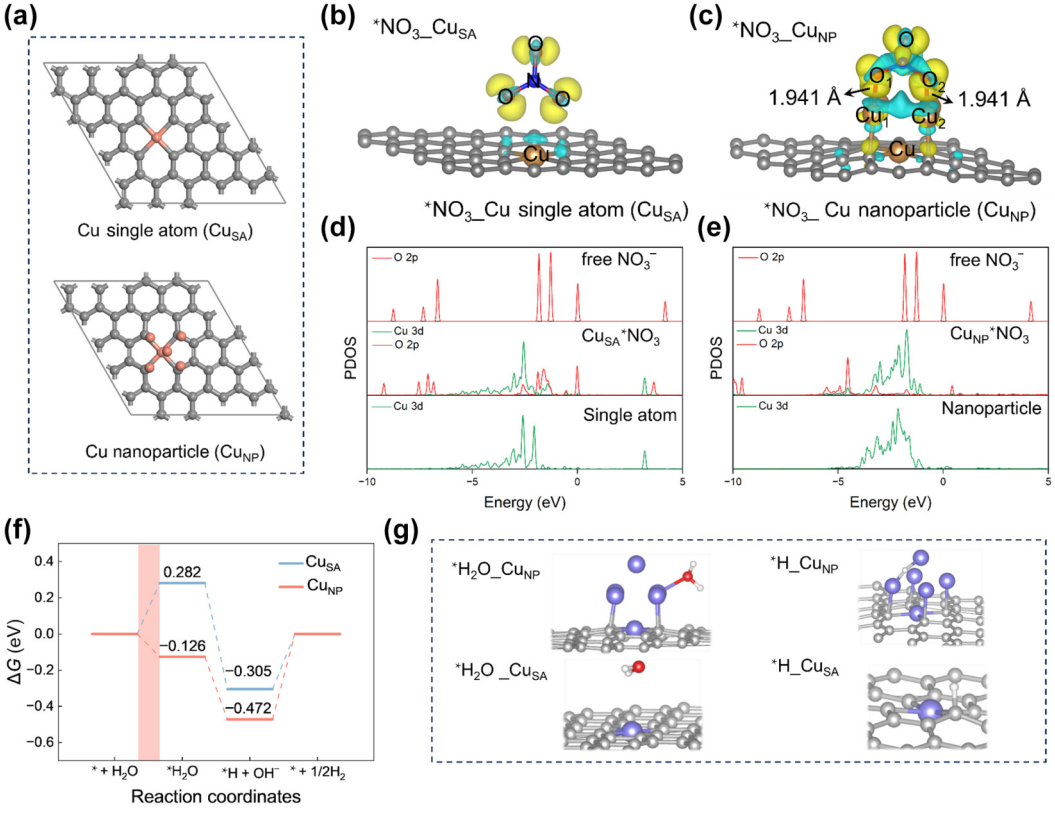

Figure 2 Structure and mechanistic studies of Cu_{SA} and Cu_{NP} co-existing in $Cu_{SA/NP}$@C. (a) Structures of Cu single-atom (Cu_{SA}) and Cu nanoparticle (Cu_{NP}). The charge density difference plots of NO_3 being adsorbed onto (b) Cu_{SA} and (c) Cu_{NP} catalysts. The yellow zones indicate charge accumulation and the cyan zones show charge depletion. Projected density of states (PDOS) for *NO_3 intermediate absorbed on Cu_{SA} (d) and Cu_{NP} (e) surfaces. (f) Gibbs free energy change of activated H supply over Cu_{SA} and Cu_{NP}. (g) The optimized geometries of the *H_2O and *H on the Cu_{SA} and Cu_{NP}, respectively.

the progress of the reaction (Figs. 4(a)–4(c)). With increasing cathodic potential, several distinct vibrational peaks emerged in the FT-IR spectra, corresponding to various nitrogen-containing intermediates. The spectral peak at 1364 cm^{-1} can be attributed to the stretching vibration mode of *NO_2H (Fig. 4(a)), providing direct evidence for the deoxygenation of nitrate during NO_3RR. The band at 1237 cm^{-1} can be attributed to the adsorption of *NO_2; notably, a blue shift of this peak was observed with increasing cathodic potential. This phenomenon is associated with the increase in *NO_2 absorption intensity, primarily due to increased *NO_2 coverage. Additionally, Figs. 4(b) and 4(c) display broad bands at 1640 and 1684 cm^{-1}, which can be assigned to the bending vibration of H_2O and σ bending of N–H, respectively. These results indicate that substantial hydrogenation reactions occur following nitrate deoxygenation, which is critical for the subsequent formation of NH_3 as the final product.

The *in-situ* electrochemical Raman experiments were conducted to reveal possible reaction intermediates in the NO_3RR process (Fig. 4(d)). The distinct peaks at 1050, 1380, and 1600 cm^{-1} were attributed to the *NO_3 stretching, antisymmetric stretching of *NO_2, and antisymmetric vibration of *NH_2, respectively [32, 39]. The peak signals of the *NO_3, *NO_2, and *NH_2 quickly increase and decrease, indicating that these intermediates were quickly consumed. To further investigate the impact of interfacial water on catalyst activity, we analyzed the *in-situ* Raman spectroscopy at 3200–3600 cm^{-1} (Fig. 4(e)). Raman peaks located at ~ 3155, ~ 3350, and ~ 3540 cm^{-1} are attributed to 4-coordinated hydrogen-bonded water (4-HB-H_2O), 2-coordinated hydrogen-bonded water (2-HB-H_2O), and K^+ ion hydrated water (K^+·H_2O), respectively [40–42]. With the application of external potential, the relative intensity of the K^+·H_2O peak gradually increases, which implies enhanced electron transfer between water molecules and the electrode surface at the solid–liquid interface. This interfacial behavior is favorable for providing active protons to drive the protonation steps of NO_3RR.

The reaction kinetics was probed by the *in-situ* EIS measurement. $Cu_{SA/NP}$@C promotes electron and ion transfer during the NO_3RR process. As is well-reported, the magnitude of the phase angle reflects the number of charges that participate in the Faraday process [43, 44]. The smaller the phase angle is, the more charges participate in the Faraday process. The Bode phase plots of the two samples manifest that, under the same bias, $Cu_{SA/NP}$@C exhibits a smaller phase angle than pure carbon felt. This means that more charges in the $Cu_{SA/NP}$@C surface participate in the Faraday reaction, instead of being stored in the electrode/electrolyte interface, while the opposite situation occurs (Fig. 4(f)). Both the *in-situ* Raman and *in-situ* EIS measurements and computational results consistently suggest that $Cu_{SA/NP}$@C has faster NO_3RR kinetics.

To gain deeper mechanistic insights into NO_3RR over the $Cu_{SA/NP}$@C catalyst, DFT calculations were performed to systematically investigate the NO_3RR activity of individual Cu_{SA} and Cu_{NP} [45]. The Gibbs free energy diagrams illustrating the possible NO_3RR reaction pathways on Cu_{SA} and Cu_{NP} are presented in Fig. 4(g), which clearly clarify the distinct reaction mechanisms on the two active components. Both Cu_{SA} and Cu_{NP} were confirmed to

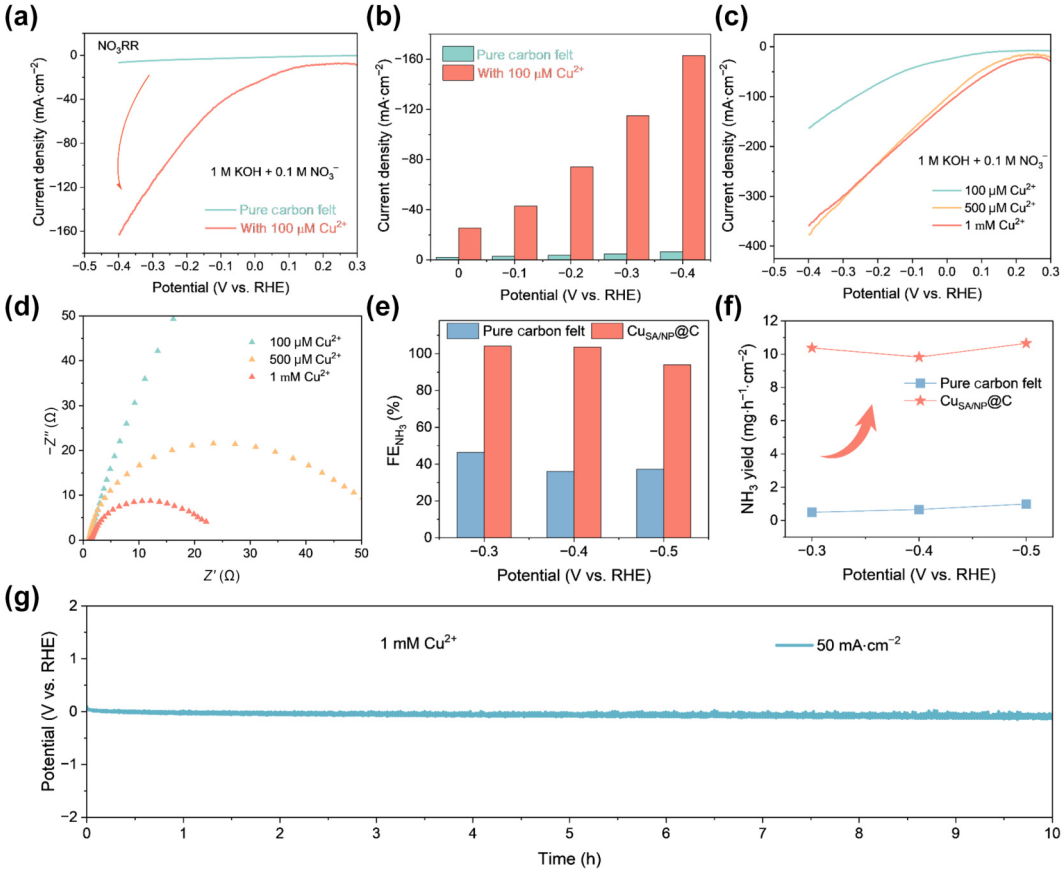

Figure 3 Electrocatalytic performance of NO_3RR by $Cu_{SA/NP}$@C. (a) LSV curves of pure carbon felt and *in-situ* prepared $Cu_{SA/NP}$@C in 1 M KOH containing 0.1 M KNO_3 with 100 μM Cu^{2+}. (b) NO_3RR current densities of pure CF and *in-situ* prepared $Cu_{SA/NP}$@C at different overpotentials. (c) LSV curves of various $Cu_{SA/NP}$@C electrocatalysts in 1 M KOH + 0.1 M KNO_3 containing different levels of Cu^{2+} (0.1, 0.5, and 1 mM). (d) Electrochemical impedance spectroscopy of different $Cu_{SA/NP}$@C and pure CF. (e) and (f) NH_3 Faradaic efficiency (e) and NH_3 yields (f) for $Cu_{SA/NP}$@C and pure CF at the given potentials. (g) Long-term stability test of $Cu_{SA/NP}$@C electrocatalyst (synthesized with 1 mM Cu^{2+}) at 50 mA·cm^{-2} at approximately 0 V (vs. RHE).

follow the *NOH-mediated reaction pathway, with the intermediate evolution sequence as follows: * + NO_3^- → *NO_3 → *NO_2 → *NO → *NOH → *NHOH → *NH_2OH → *NH_2 → *NH_3. Notably, significant differences were observed in the initial NO_3^- adsorption step between Cu_{SA} and Cu_{NP}. On Cu_{NP}, the NO_3^- adsorption is a thermodynamically favorable process with a Gibbs free energy change of −1.48 eV; in contrast, this step is non-spontaneous on Cu_{SA}, exhibiting a positive endergonic free energy change of 1.30 eV. For Cu_{SA}, this initial * + NO_3^- → *NO_3 step thus acts as the potential-determining step (PDS) for the entire NO_3RR process, as it imposes the highest thermodynamic barrier. In comparison, the PDS of Cu_{NP} for NO_3RR exhibits a Gibbs free energy barrier that is 0.84 eV lower than that of Cu_{SA}. This substantial reduction in the PDS barrier explains why Cu_{NP} contributes to accelerated NO_3RR kinetics, while the synergistic combination of Cu_{SA} (suppressing HER and enhancing selectivity) and Cu_{NP} (lowering PDS barrier and promoting activity) ultimately endows the $Cu_{SA/NP}$@C catalyst with its superior overall NO_3RR performance.

2.5 Continuous production of ammonia in MEA reactor

To investigate practical applications of $Cu_{SA/NP}$@C catalyst for ammonia synthesis, we constructed an electro-refinery using an MEA-based electrolyzer (Fig. 5(a)) [46–49]. As shown in Fig. 5(b), after changing the cathode catalyst from pure carbon felt to CuSA/NP@C, the cell voltage decreased by approximately 100 mV at the current density of 500 mA·cm^{-2}. The current density of $Cu_{SA/NP}$@C has significantly increased at different full battery voltages (Fig. 5(c)). Furthermore, the $Cu_{SA/NP}$@C catalyst maintained excellent stability at industrial-level 200 mA·cm^{-2} for over 90 h (Fig. 5(d)). This result indicates the industrial prospects of the "waste to wealth" transformation route with $Cu_{SA/NP}$@C for the NO_3RR.

3 Conclusions

In summary, our study addresses the issues of high catalyst cost and limited practical wastewater application in NO_3RR for ammonia synthesis by proposing a "treating waste with waste" strategy. A $Cu_{SA/NP}$@C catalyst was prepared via *in-situ* electrochemical deposition directly from copper-containing wastewater. The effect of different Cu^{2+} concentrations was investigated, and the catalyst fabricated at 500 μM exhibited excellent performance due to the synergy between single atoms and nanoparticles: a NH_3 Faradaic efficiency of ~ 100% and a NH_3 yield of 10 mg·cm^{-2} at −0.3 V vs. RHE. DFT calculations and *in-situ* characterizations confirmed that the two components respectively regulate *H behavior and reduce reaction energy barriers. A membrane electrode assembly achieved stable NH_3 synthesis at an industrial current density of 200 mA·cm^{-2} for over 90 h, providing a new path for wastewater recycling and green ammonia synthesis.

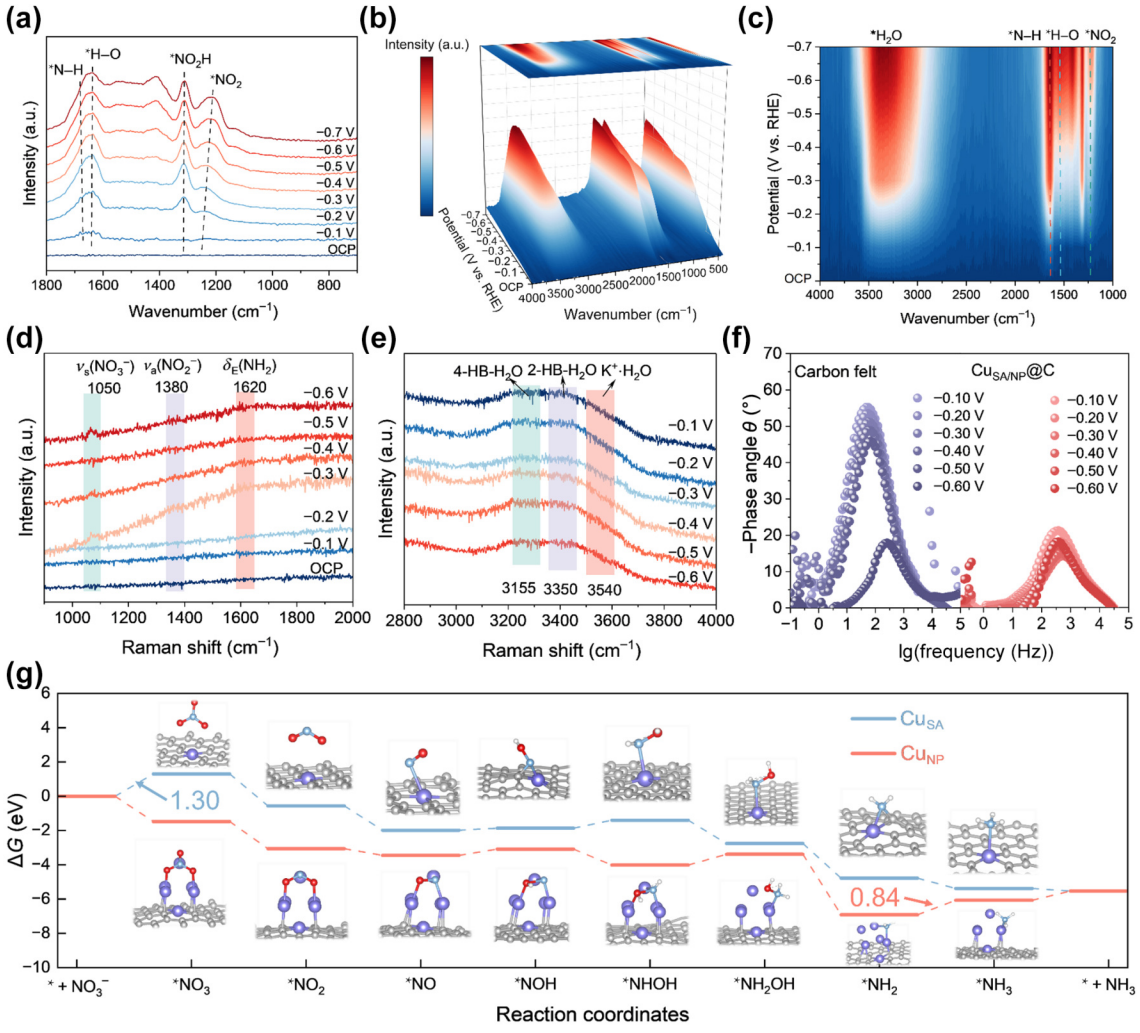

Figure 4 NO_3RR mechanism studies by *in-situ* characterization and theoretical calculations. (a) *In-situ* FT-IR spectra of CuSA/NP@C under different potentials (open circuit potential (OCP) = −0.7 V vs. RHE) of NO_3RR. (b) and (c) Three-dimensional (3D) map of the *in-situ* FT-IR spectra of $Cu_{SA/NP}$@C under different potentials (OCP = −0.7 V vs. RHE) of NO_3RR. (d) and (e) *In-situ* Raman spectra of $Cu_{SA/NP}$@C during NO_3RR at different potentials. (f) Bode phase plots of $Cu_{SA/NP}$@C and pure carbon felt for NO_3RR at different potentials. (g) Free-energy profiles for the most thermodynamically favorable pathway of NO_3RR on Cu_{SA} and Cu_{NP}.

4 Methods

4.1 $Cu_{SA/NP}$@C synthesis

Copper nitrate (0.01, 0.05, and 0.1 mmol) was dissolved in deionized water (100 mL) containing KOH (100 mmol) and KNO_3 (10 mmol) at room temperature. The catalyst was prepared by electrochemical *in-situ* deposition, which involved conducting CV measurements on carbon felt (geometric area: 1 cm × 1 cm). The electrolyte used was 1 M KOH supplemented with 0.1 M KNO_3 and Cu^{2+} ions (at the concentrations of 100, 500, and 1000 μM), and the CV cycling was carried out over a range from the 1st to the 300th cycles. During the electrochemical *in-situ* deposition, the CV scan rate was set to 100 mV·s^{-1}, and the potential window was controlled at −0.4 to 0.3 V vs. RHE.

4.2 Electrochemical measurements

Electrochemical measurements were performed in a standard three-electrode system (Jiangsu BOKE New Materials Technology Co., LTD.) using a CHI 760E electrochemical workstation. A $Hg/HgCl_2$ electrode and a graphite rod were used as the reference electrode and counter electrode, respectively. Fumasep FAB-PK-130 was used as an anion exchange membrane (AEM), provided by Jiangsu BOKE Co., LTD. All the potentials vs. $Hg/HgCl_2$ were converted to the values versus RHE according to the equation (E vs. RHE = E vs. $Hg/HgCl_2$ + 0.0592 × pH + 0.244 V). LSV polarization curves were recorded at a scan rate of 5 mV·s^{-1} and 500 rpm. For the catalytic potential, the *iR* correction was not used. Before the LSV test, ten cycles of cyclic voltammetry measurements were conducted (100 mV·s^{-1}) to clean the catalyst surface. Unless otherwise stated, all linear voltammetry curves were recorded after three prescans to achieve stabilization.

4.3 MEA tests in a paired electro-refinery

For testing in a flow electrolyzer (Model: BKT2-SN-22-8X, manufactured by Jiangsu BOKE Co., Ltd., China), an MEA was prepared by sandwiching the $Cu_{SA/NP}$@C cathode and Ni mesh anode between a commercial membrane (Fumasep FAB-PK-130). The test was conducted at a room temperature of 25 ± 2 °C. The MEA was then placed within a custom-designed electrolyzer where 1 M KOH with 0.1 M KNO_3 solution as the catholyte and 1 M KOH as the anolyte were circulated through cathode and anode, respectively, at a flow rate of 60 mL·min^{-1}.

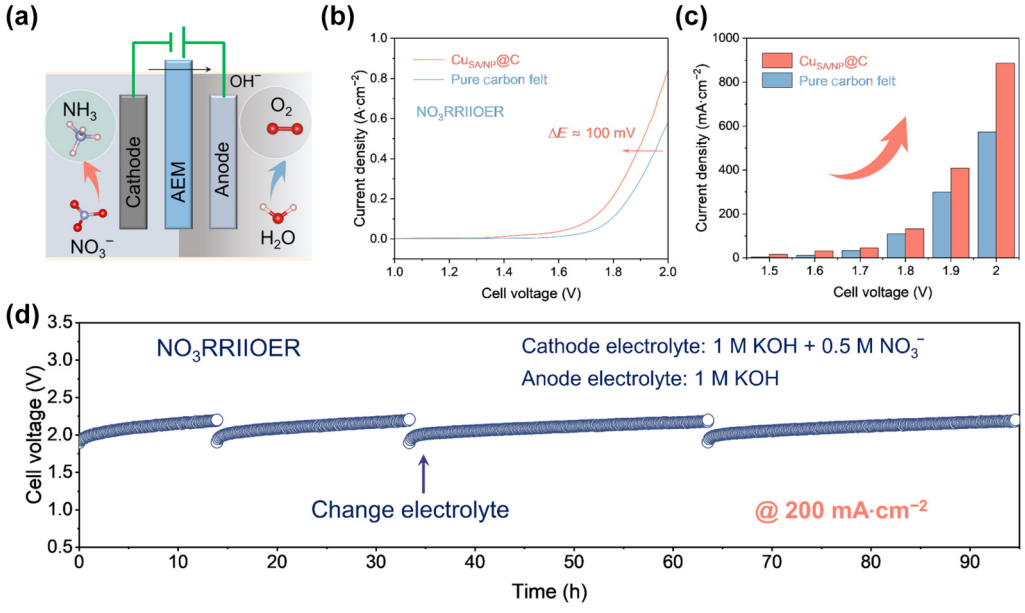

Figure 5 MEA-based electrolyzer performance. (a) Schematic illustration of MEA electrolyzer. (b) *V*–*I* curves of MEA electrolyzer assembled with $Cu_{SA/NP}$@C or pure carbon felt as the cathode. (c) Current densities of $Cu_{SA/NP}$@C and pure carbon felt at 1.5–2 V for NO_3RR||OER. (d) Continuous tests of the $Cu_{SA/NP}$@C catalyst at industrial 200 mA·cm^{-2} for over 90 h using a MEA-based electrolyzer for ammonia production.

4.4 *In-situ* Raman analyses

In-situ Raman spectra were recorded on a micro-Raman spectrometer (Renishaw) under an excitation of 532 nm laser light at controlled potentials by the CHI 630E electrochemical workstation. The electrochemical *operando* Raman cell was provided by Beijing Scistar Technology Co., Ltd. In addition, $Cu_{SA/NP}$@C deposited on glassy carbon was used as a working electrode. A Pt wire as the counter electrode was rolled to a circle around the cell. The Ag/AgCl electrode (sat. KCl) was used as the reference electrode. The *in-situ* Raman spectra were collected under chronoamperometry (*I*–*t*) at different potentials in 1 M KOH with 0.1 M KNO_3 solution.

4.5 *In-situ* FT-IR analyses

The *in-situ* infrared spectroscopy measurements were carried out on a Nicolet 6700 FT-IR spectrometer (Thermo Scientific, USA) equipped with a liquid-nitrogen cooled MCT-A detector. For continuous collection of *in-situ* FT-IR spectra during NO_3RR, the $Cu_{SA/NP}$@C catalyst served as the working electrode. A saturated Hg/HgO electrode and a Pt wire were used as the reference and counter electrodes, respectively. The electrochemical cell was filled with the specific reaction solution. Each spectrum was scanned 32 times with a spectral resolution of 4 cm^{-1} and a time interval of 0.2 min during the electrochemical reduction process.

4.6 Detection of NH_4^+

The quantification of NH_4^+ was conducted with Nessler's reagent as the coloring agent [50]. 1 mL of electrolyte after NO_3RR was first taken out from the cathodic compartment and diluted to 5 mL. Then potassium sodium tartrate solution (500 g·L^{-1}, 0.1 mL) was added and thoroughly mixed. In the last step, 0.1 mL of Nessler's reagent was added to the above mixture. After being left standing for 20 min, the absorbance at 420 nm was measured by ultraviolet (UV)-spectroscopy (PG2000-Pro back-thinned spectrometer, ideaoptics, China). The obtained value was then fitted to the calibration curve to acquire the corresponding NH_4^+ concentration.

4.7 Calculation of NH_3 Faradaic efficiency

The NH_3 Faradaic efficiency was calculated according to

$$FE_{NH_3} = \frac{Q_{NH_3}}{Q} = \frac{n_{NH_3} V_{NH_3} F}{Q} \quad (1)$$

where Q represents the applied overall Coulomb quantity (C), Q_{NH_3} is the Coulomb quantity required to produce NH_3, n is the electron-transfer number (for 1 mol NH_3, it is 8), V is the volume of the catholyte of the cathode chamber (30 mL), C_{NH_3} is the concentration of NH_3 produced, and F is the Faraday constant (96,485 C·mol^{-1}).

4.8 Computational and simulation details

DFT calculations were performed using the Vienna *ab initio* simulation package (VASP) [51], employing the generalized gradient approximation (GGA) [52] with the Perdew–Burke–Ernzerhof (PBE) exchange-correlation functional [53]. A plane-wave energy cutoff of 450 eV and a 3 × 3 × 1 Monkhorst–Pack grid for *k*-point sampling were set to ensure numerical precision. Convergence criteria were established at 10^{-5} eV for energy and 0.05 eV·Å^{-1} for forces. Grimme's DFT-D3 dispersion correction was incorporated to account for long-range van der Waals interactions [54]. A vacuum layer of 15 Å thickness was added in the *z* direction to avoid spurious interactions between periodic images. The CDD was plotted using the VESTA program [55]. The Gibbs free energy changes (ΔG) for each elementary steps were based on the computational hydrogen electrode (CHE) model [56], which could be calculated by the following equation

$$\Delta G = \Delta E + \Delta ZPE - T\Delta S \quad (2)$$

where ΔE is obtained directly from DFT calculations, ΔZPE is the change of zero-point energies (ZPE), T is the temperature of 298.15 K, and ΔS is the entropy change.

Electronic Supplementary Material: Supplementary material (information of the experimental characterization, SEM images, TEM images, UV–Vis absorption spectra, and FEd of different samples, CV curves, and *I–t* curves) is available in the online version of this article at https://doi.org/10.26599/NR.2026.94908370.

Data availability

All data needed to support the conclusions in the paper are presented in the manuscript and the Electronic Supplementary Material. Additional data related to this paper may be requested from the corresponding author upon request.

Acknowledgements

The authors are grateful for the financial support from the National Natural Science Foundation of China (Nos. 52472231, 52311530113, and W2521017) and the Central Guidance on Science and Technology Development Fund of Zhejiang Province (No. 2024ZY01011).

Declaration of competing interest

All the contributing authors report no conflict of interests in this work.

Author contribution statement

Z. R. L. and J. J. W.: Data curation, project administration, validation, writing manuscript, experimental design. Y. F. L.: Data curation, validation. C. L. Q.: DFT calculations, writing manuscript. Y. H. L. and J. C. W.: Project administration, funding acquisition, writing manuscript. All the authors have approved the final manuscript.

Use of AI statement

During the preparation of this work, the authors used ChatGPT in order to polish the grammar. After using this tool/service, the authors reviewed and edited the content as needed and take full responsibility for the content of the publication.

References

[1] De Luna, P.; Hahn, C.; Higgins, D.; Jaffer, S. A.; Jaramillo, T. F.; Sargent, E. H. What would it take for renewably powered electrosynthesis to displace petrochemical processes. *Science* **2019**, *364*, eaav3506.

[2] Chu, S.; Majumdar, A. Opportunities and challenges for a sustainable energy future. *Nature* **2012**, *488*, 294–303.

[3] Seh, Z. W.; Kibsgaard, J.; Dickens, C. F.; Chorkendorff, I.; Nørskov, J. K.; Jaramillo, T. F. Combining theory and experiment in electrocatalysis: Insights into materials design. *Science* **2017**, *355*, eaad4998.

[4] Liu, M.; Pang, Y. J.; Zhang, B.; De Luna, P.; Voznyy, O.; Xu, J. X.; Zheng, X. L.; Dinh, C. T.; Fan, F. J.; Cao, C. H. et al. Enhanced electrocatalytic CO_2 reduction via field-induced reagent concentration. *Nature* **2016**, *537*, 382–386.

[5] Kyriakou, V.; Garagounis, I.; Vourros, A.; Vasileiou, E.; Stoukides, M. An electrochemical Haber-Bosch process. *Joule* **2020**, *4*, 142–158.

[6] Ma, A. J.; Gui, J. Z.; Huang, Y. M.; Yu, Y. F. Electrocatalytic coupling of anodic nitrogen oxidation and cathodic nitrate reduction for ammonia synthesis from air and water. *Nano Res.* **2024**, *17*, 7824–7829.

[7] van Langevelde, P. H.; Katsounaros, I.; Koper, M. T. M. Electrocatalytic nitrate reduction for sustainable ammonia production. *Joule* **2021**, *5*, 290–294.

[8] Lin, G. X.; Ju, Q. J.; Guo, X. W.; Zhao, W.; Adimi, S.; Ye, J. Y.; Bi, Q. Y.; Wang, J. C.; Yang, M. H.; Huang, F. Q. Intrinsic electron localization of metastable MoS_2 boosts electrocatalytic nitrogen reduction to ammonia. *Adv. Mater.* **2021**, *33*, 2007509.

[9] Li, S. L.; Ma, P. J.; Gao, C. L.; Liu, L. J.; Wang, X. L.; Shakouri, M.; Chernikov, R.; Wang, K. W.; Liu, D. M.; Ma, R. G. et al. Reconstruction-induced NiCu-based catalysts towards paired electrochemical refining. *Energy Environ. Sci.* **2022**, *15*, 3004–3014.

[10] Chen, F. Y.; Elgazzar, A.; Pecaut, S.; Qiu, C.; Feng, Y. G.; Ashokkumar, S.; Yu, Z.; Sellers, C.; Hao, S. Y.; Zhu, P. et al. Electrochemical nitrate reduction to ammonia with cation shuttling in a solid electrolyte reactor. *Nat. Catal.* **2024**, *7*, 1032–1043.

[11] Han, S. H.; Li, H. J.; Li, T. L.; Chen, F. P.; Yang, R.; Yu, Y. F.; Zhang, B. Ultralow overpotential nitrate reduction to ammonia via a three-step relay mechanism. *Nat. Catal.* **2023**, *6*, 402–414.

[12] Wang X. L.; Wang J. C.; Hu H. S.; Yin C. L.; Chang L.-Y.; Zhu Y.; Wang J. C.; Yang M. H. Harnessing spin-lattice interplay in metal nitrides for efficient ammonia electrosynthesis. *Adv. Mater.* **2025**, *37*, 2504505.

[13] Liao, W. R.; Wang, J.; Ni, G. H.; Liu, K.; Liu, C. X.; Chen, S. Y.; Wang, Q. Y.; Chen, Y. K.; Luo, T.; Wang, X. Q. et al. Sustainable conversion of alkaline nitrate to ammonia at activities greater than 2 $A \cdot cm^{-2}$. *Nat. Commun.* **2024**, *15*, 1264.

[14] Zhang, B. C.; Dai, Z. C.; Chen, Y. X.; Cheng, M. Y.; Zhang, H. K.; Feng, P. Y.; Ke, B. Q.; Zhang, Y. Y.; Zhang, G. Q. Defect-induced triple synergistic modulation in copper for superior electrochemical ammonia production across broad nitrate concentrations. *Nat. Commun.* **2024**, *15*, 2816.

[15] Wu, Z. Y.; Kang, X. X.; Wang, S.; Song, Y. H.; Xie, F. T.; Duan, X. M.; Yang, J. P. Co-catalytic metal–support interactions design on single-atom alloy for boosted electro-reduction of nitrate to nitrogen. *Adv. Funct. Mater.* **2024**, *34*, 2406917.

[16] Sun, Y. H.; Chen, J. X.; Du, X. M.; Cui, J. W.; Chen, X.; Wu, C. H.; Yang, X. M.; Liu, L. Q.; Ye, J. H. Anchoring Cs^+ ions on carbon vacancies for selective CO_2 electroreduction to CO at high current densities in membrane electrode assembly electrolyzers. *Angew. Chem., Int. Ed.* **2024**, *63*, e202410802.

[17] Xiong Y. C.; Wang Y. H.; Zhou J. W.; Liu F.; Hao F. K.; Fan Z. X. Electrochemical nitrate reduction: Ammonia synthesis and the beyond. *Adv. Mater.* **2024**, *36*, 2304021.

[18] Wang, J. J.; Lv, X. M.; Ma, J. Q.; Du, H. X.; Lv, Z. R.; Wang, J. C.; Huang, F. Q. Tailoring the delocalization state in electrocatalysts for efficient NO_x reduction: Recent advances and perspectives. *ACS Catal.* **2025**, *15*, 19175–19191.

[19] Chen, F. Y.; Wu, Z. Y.; Gupta, S.; Rivera, D. J.; Lambeets, S. V.; Pecaut, S.; Kim, J. Y. T.; Zhu, P.; Finfrock, Y. Z.; Meira, D. M. et al. Efficient conversion of low-concentration nitrate sources into ammonia on a Ru-dispersed Cu nanowire electrocatalyst. *Nat. Nanotechnol.* **2022**, *17*, 759–767.

[20] Chen, G. F.; Yuan, Y. F.; Jiang, H. F.; Ren, S. Y.; Ding, L. X.; Ma, L.; Wu, T. P.; Lu, J.; Wang, H. H. Electrochemical reduction of nitrate to ammonia via direct eight-electron transfer using a copper-molecular solid catalyst. *Nat. Energy* **2020**, *5*, 605–613.

[21] Wang, J. C.; Ma, J. Q.; Du, H. X.; Ma, R. G.; Wang, J. C. Electrifying nitrate conversion: Dual-metal-site catalysts as a game-changer for sustainable NH_3 production. *Nano Res.* **2026**, *19*, 94907798.

[22] Hua, Y. L.; Song, N.; Wu, Z. Y.; Lan, Y.; Luo, H. X.; Song, Q. Q.; Yang, J. P. Cu-Fe synergistic active sites boost kinetics of electrochemical nitrate reduction. *Adv. Funct. Mater.* **2024**, *34*, 2314461.

[23] Zhou, B.; Tong, Y. W.; Yao, Y. C.; Zhang, W. X.; Zhan, G. M.; Zheng, Q.; Hou, W.; Gu, X. K.; Zhang, L. Z. Reversed I_1Cu_4 single-atom sites for superior neutral ammonia electrosynthesis with nitrate. *Proc. Natl. Acad. Sci. USA* **2024**, *121*, e2405236121.

[24] Cheng, X. F.; He, J. H.; Ji, H. Q.; Zhang, H. Y.; Cao, Q.; Sun, W. J.; Yan, C. L.; Lu, J. M. Coordination symmetry breaking of single-atom catalysts for robust and efficient nitrate electroreduction to ammonia. *Adv. Mater.* **2022**, *34*, 2205767.
[25] Hu, Q.; Shang, C. Y.; Chen, X. B.; Qi, S.; Huo, Q. H.; Yang, H. P.; He, C. X. Subnanometric nickel phosphide heteroclusters with highly active $Ni^{\delta+}$–$P^{\delta-}$ pairs for nitrate reduction toward ammonia. *J. Am. Chem. Soc.* **2025**, *147*, 12228–12238.
[26] Yu, M.; Huang, H.; Hu, J.; Fan, B.; Wang, S. Interfacial engineering of molybdenum disulfide by vanadium-MXene for efficient electrochemical nitrate reduction. *Nano Res.* **2025**, *18*, 94907521.
[27] Qi, S.; Lei, Z. H.; Huo, Q. H.; Zhao, J. W.; Huang, T. C.; Meng, N.; Liao, J. L.; Yi, J. B.; Shang, C. Y.; Zhang, X. et al. Ultrathin high-entropy Fe-based spinel oxide nanosheets with metalloid band structures for efficient nitrate reduction toward ammonia. *Adv. Mater.* **2024**, *36*, 2403958.
[28] Gong, Z. H.; Xiang, X. P.; Zhong, W. Y.; Jia, C. H.; Chen, P. Y.; Zhang, N.; Zhao, S. J.; Liu, W. Z.; Chen, Y.; Lin, Z. Modulating metal-nitrogen coupling in anti-perovskite nitride via cation doping for efficient reduction of nitrate to ammonia. *Angew. Chem., Int. Ed.* **2023**, *62*, e202308775.
[29] Guo, C. Y.; Shen, L. Y.; Tang, Y. J.; Chen, M. Y.; Zhou, X. X.; Ciucci, F.; Tang, Z. H. Ru single atoms anchored on Co-NC for nitrate electroreduction toward NH_3 synthesis. *Nano Res.* **2025**, *18*, 94907623.
[30] Liu, Y. L.; Zheng, Z. Y.; Jabeen, S.; Liu, N. Y.; Liu, Y. X.; Cheng, Y. Y.; Li, Y. X.; Yu, J. W.; Wu, X.; Yan, N. N. et al. Mechanochemical route to fabricate an efficient nitrate reduction electrocatalyst. *Nano Res.* **2024**, *17*, 4889–4897.
[31] Zhang, F. Z.; Luo, J. M.; Chen, J. L.; Luo, H. X.; Jiang, M. M.; Yang, C. X.; Zhang, H.; Chen, J.; Dong, A. G.; Yang, J. P. Interfacial assembly of nanocrystals on nanofibers with strong interaction for electrocatalytic nitrate reduction. *Angew. Chem., Int. Ed.* **2023**, *62*, e202310383.
[32] Zhang, L. H.; Jia, Y. T.; Zhan, J. Y.; Liu, G. M.; Liu, G. H.; Li, F.; Yu, F. S. Dopant-induced electronic states regulation boosting electroreduction of dilute nitrate to ammonium. *Angew. Chem., Int. Ed.* **2023**, *62*, e202303483.
[33] Aminu, A.; Pirzada, B. M.; Talib, S. H.; Shaya, J.; Yildiz, I.; Sharmarke Mohamed, S.; Qurashi, A. Fe foam supported $FeVO_4$ nanoparticles for electrochemical nitrogen fixation at ambient conditions. *Nano Res. Energy* **2025**, *4*, e9120161.
[34] Chen, Y. P.; Wu, Y. C.; Sun, Z. F.; Gao, G. Y.; Hu, X. C.; Zhang, Y. G.; Luo, Q.; Wang, L. S.; Peng, D.-L.; Wang, M.-S. et al. Unraveling Enhanced Conversion Reversibility of Regulated Cu4SnS4 Composites for Superior Lithium Storage. *Nano Res. Energy* **2025**, *4*, e9120192.
[35] Chen, H.; Liu, M. Y.; Jiang, Z. J.; Sun, S. J.; Shakir, I.; Hou, S.; Sun, X. P. Achieving durable alkaline seawater oxidation over NiFe layered double hydroxide via sulfur doping. *Nano Res. Energy* **2025**, *4*, e9120211.
[36] Zhu, H. B.; Wang, J. J.; Xu, Z. A.; Tan, Y. W.; Wang, J. C. Pd nanoparticle size-dependent H* coverage for Cu-catalyzed nitrate electro-reduction to ammonia in neutral electrolyte. *Small* **2024**, *20*, 2404919.
[37] Fang, J. Y.; Zheng, Q. Z.; Lou, Y. Y.; Zhao, K. M.; Hu, S. N.; Li, G.; Akdim, O.; Huang, X. Y.; Sun, S. G. Ampere-level current density ammonia electrochemical synthesis using CuCo nanosheets simulating nitrite reductase bifunctional nature. *Nat. Commun.* **2022**, *13*, 7899.
[38] Wang, Y. T.; Zhou, W.; Jia, R. R.; Yu, Y. F.; Zhang, B. Unveiling the activity origin of a copper-based electrocatalyst for selective nitrate reduction to ammonia. *Angew. Chem., Int. Ed.* **2020**, *59*, 5350–5354.
[39] Wang, J. C.; Bui, H. T. D.; Hu, H. S.; Kong, S. Y.; Wang, X. L.; Zhu, H. B.; Ma, J. Q.; Xu, J. T.; Liu, Y. H.; Liu, L. J. et al. Industrial-current ammonia synthesis by polarized cuprous cyanamide coupled to valorization of glycerol at 4,000 $mA \cdot cm^{-2}$. *Adv. Mater.* **2025**, *37*, 2418451.
[40] Deng, L. M.; Chen, H. J.; Hung, S. F.; Zhang, Y.; Yu, H. Z.; Chen, H. Y.; Li, L. L.; Peng, S. J. Lewis acid-mediated interfacial water supply for sustainable proton exchange membrane water electrolysis. *J. Am. Chem. Soc.* **2024**, *146*, 35438–35448.
[41] Zhang, S. N.; Gao, P.; Liu, Q. Y.; Zhang, Z.; Leng, B. L.; Chen, J. S.; Li, X. H. Ampere-level reduction of pure nitrate by electron-deficient Ru with K^+ ions repelling effect. *Nat. Commun.* **2024**, *15*, 10877.
[42] Du, H. X.; Li, H.; Song, J. N.; Wang, X. L.; Wang, J. C.; Ma, J. Q.; Ran, N.; Yu, S. L.; Yang, M. H.; Jin, Y. X. et al. Reconstructing interfacial H-bond networks via surface lewis-base silicate species for durable seawater oxidation. *Adv. Funct. Mater.*, in press, https://doi.org/10.1002/adfm.202525265.
[43] Hu, Q.; Qi, S.; Huo, Q. H.; Zhao, Y. X.; Sun, J. J.; Chen, X. B.; Lv, M. Y.; Zhou, W. L.; Feng, C.; Chai, X. Y. et al. Designing efficient nitrate reduction electrocatalysts by identifying and optimizing active sites of Co-based spinels. *J. Am. Chem. Soc.* **2023**, *146*, 2967–2976.
[44] Wang, J. J.; Bui, H. T. D.; Wang, X. L.; Lv, Z. R.; Hu, H. S.; Kong, S. Y.; Wang, Z. Q.; Liu, L. J.; Chen, W.; Bi, H. et al. A copper-zinc cyanamide solid-solution catalyst with tailored surface electrostatic potentials promotes asymmetric N-intermediate adsorption in nitrite electroreduction. *J. Am. Chem. Soc.* **2025**, *147*, 8012–8023.
[45] Qiu, C. L.; Brinck, T.; Wang, J. C. Modeling the potential energy surface by force fields for heterogeneous catalysis: Classification, applications, and challenges. *Chem. Sci.* **2025**, *16*, 21269–21297.
[46] Feng, Y. H.; Ran, N.; Wang, X. L.; Liu, Q. N.; Wang, J. C.; Liu, L. J.; Suenaga, K.; Zhong, W. W.; Ma, R. G.; Liu, J. J. Nanoparticulate WN/Ni_3C coupling in ceramic coatings for boosted urea electro-oxidation. *Adv. Energy Mater.* **2023**, *13*, 2302452.
[47] Feng, Y. H.; Wang, X. L.; Ma, J. Q.; Wang, N.; Liu, Q. N.; Suenaga, K.; Chen, W.; Zhang, J. T.; Zhou, Y.; Wang, J. C. A solid-solution with asymmetric Ni–O–Cr sites for boosting protonation toward anodic oxidation. *Adv. Energy Mater.* **2024**, *14*, 2401501.
[48] Yu, Y.; Ma, J. Q.; Zhang, L. L.; Sun, T. M.; Wang, M. M.; Zhu, J. L.; Wang, J. C. Selective electrooxidation of 5-hydroxymethylfurfural to value-added 2,5-furanodiformic acid: Mechanism, electrolyzer system, and electrocatalyst regulation. *Chem. Commun.* **2025**, *61*, 7751–7769.
[49] Yao, Z. J.; Cheng, Z. J.; Zhang, L. L.; Wang, J. C. Electrocatalytic CO_2 reduction in acidic media: From fundamental challenges to sustainable solutions. *Adv. Sustain. Syst.* **2025**, *9*, e01236.
[50] Deng, X. H.; Yang, Y.P.; Wang, L.; Fu, X. Z.; Luo, J. L. Metallic Co nanoarray catalyzes selective NH_3 production from electrochemical nitrate reduction at current densities exceeding 2 $A \cdot cm^{-2}$. *Adv. Sci.* **2021**, *8*, 2004523.
[51] Kresse, G.; Furthmüller, J. Efficient iterative schemes for *ab initio* total-energy calculations using a plane-wave basis set. *Phys. Rev. B* **1996**, *54*, 11169–11186.
[52] Blöchl, P. E. Projector augmented-wave method. *Phys. Rev. B* **1994**, *50*, 17953–17979.
[53] Perdew, J. P.; Burke, K.; Ernzerhof, M. Generalized gradient approximation made simple. *Phys. Rev. Lett.* **1996**, *77*, 3865–3868.
[54] Grimme, S.; Antony, J.; Ehrlich, S.; Krieg, H. A consistent and accurate *ab initio* parametrization of density functional dispersion correction (DFT-D) for the 94 elements H-Pu. *J. Chem. Phys.* **2010**, *132*, 154104.
[55] Momma, K.; Izumi, F. *VESTA* 3 for three-dimensional visualization of crystal, volumetric and morphology data. *J. Appl. Cryst.* **2011**, *44*, 1272–1276.
[56] Nørskov, J. K.; Rossmeisl, J.; Logadottir, A.; Lindqvist, L.; Kitchin, J. R.; Bligaard, T.; Jónsson, H. Origin of the overpotential for oxygen reduction at a fuel-cell cathode. *J. Phys. Chem. B* **2004**, *108*, 17886–17892.

This is an open access article under the terms of the Creative Commons Attribution 4.0 International License (CC BY 4.0, https://creativecommons.org/licenses/by/4.0/).

© The Author(s) 2026. Published by Tsinghua University Press.